

<https://doi.org/10.1038/s43247-025-03081-8>

Climate and sedimentary structure drive deep labile carbon accumulation in alpine wetlands

Check for updates

Youqing Yang^{1,2,8}, Xiaoping Wang^{3,8}, Jianqing Du^{2,4,5,9}✉, Hui Zhang⁶, Zhixiang Niu^{2,5}, Yitao Zhang⁵, Zeyuan Wang¹, Liyuan Ma⁵, Haijun Zhang⁵, Danhong Chen¹, Chenhao Gao¹, Qiang Liu⁵, Yu Wu⁵, Yanbin Hao^{1,2,4}, Haishan Niu^{2,5}, Kai Xue^{2,4,5}, Xiaoyong Cui^{1,2,9}✉ & Yanfen Wang^{2,5,7}

Wetlands serve as vital carbon sinks; however, compared with the surface carbon pool, the relative stock and stability of organic carbon (OC) buried in deep sediment layers remain uncertain, particularly in alpine regions. Based on 42 sediment across seven wetlands on the Qinghai-Xizang Plateau, this study disentangled the OC accumulation process and its drivers since the Holocene. Our results highlighted that deep sediments (>1 m) stored ~70% of the total OC in alpine wetlands, much of which was labile. Historical warming facilitated the accumulation of such labile OC. Moreover, an intercalated sedimentary structure, formed by silt and fine-grained clay both below and above the OC-rich layer, prevented them from rapid decomposition. Given that elevated groundwater temperatures and intensified hydrological processes in alpine regions may stimulate the decomposition of these massive labile OC pools, releasing carbon into surface water or the atmosphere, future climate change assessments should take this long-overlooked carbon pool into account.

Although wetlands cover only 5%–8% of the global terrestrial area, they contribute 20%–30% of the global organic carbon (OC) stock in soils^{1–3}. As OC in wetlands generally accumulates in the surface layer from plant and aquatic inputs, most research focuses on surface sediment layers^{3,4}. The OC stock in deeper sediment layers (> 1 m) remains highly controversial. Some studies suggest that it is typically low^{5,6}, while other studies have shown that under specific geological historical sedimentation conditions (such as the Holocene thermal maximum), the amount of OC inputs into sediments may exceed that in the modern surface sediments, resulting in higher OC stocks in deep sediments^{3,7,8}.

The primary reason that deep OC is often overlooked may lie in its “recalcitrance”. Generally, OC stability increases with burial depth due to a higher proportion of recalcitrant compounds and aromatic structures that resist decomposition⁹. Moreover, the anoxic (or anaerobic) and relatively cold conditions limit microbial metabolic activity and reduce the carbon decomposition rate. However, significant uncertainties persist regarding the OC stability of deep wetland sediments. For instance, in alpine wetlands

with high anaerobic conditions, the aliphatic content increases with depth in catotelm layers, indicating a relative decrease in OC stability in deeper layers^{10,11}. These uncertainties may stem from environmental factors such as climate and burial conditions. Climate modulates sediment OC stability by altering hydrological conditions, plant communities, and associated ecological processes through changes in temperature and precipitation^{3,10,12–14}. Burial conditions, shaped by topography and long-term sedimentation, determine the storage environment of OC, thereby regulating its decomposition dynamics^{15,16}. The effects of this factor manifest over centennial timescales and have been largely overlooked in ecological research. Once deeply buried (i.e., during flooding), OC decomposition rates may decrease, leading to an increased organic carbon accumulation rate (OCAR)^{16,17}. For example, fine grained sediments, such as clay and silt, provide better adsorption and aggregation sites for labile OC, thereby reducing microbial decomposition and preserving OC lability¹⁸. Nevertheless, the specific mechanisms through which historical climate fluctuations and hydrological regimes have collectively influenced sedimentary carbon sources and burial

¹College of Life Sciences, University of Chinese Academy of Sciences, Beijing, China. ²Beijing Yanshan Earth Critical Zone National Research Station, University of Chinese Academy of Sciences, Beijing, China. ³International Joint Research Laboratory for Global Change Ecology, School of Life Sciences, Henan University, Kaifeng, China. ⁴National Key Laboratory of Earth System Numerical Modeling and Application, Chinese Academy of Sciences, Beijing, China. ⁵College of Resources and Environment, University of Chinese Academy of Sciences, Beijing, China. ⁶State Key Laboratory of Lithospheric and Environmental Coevolution, Institute of Geology and Geophysics, Chinese Academy of Sciences, Beijing, China. ⁷State Key Laboratory of Tibetan Plateau Earth System, Environment and Resources, Chinese Academy of Sciences, Beijing, China. ⁸These authors contributed equally: Youqing Yang, Xiaoping Wang. ⁹These authors jointly supervised this work: Jianqing Du, Xiaoyong Cui. ✉e-mail: jqdu@ucas.ac.cn; cuixy@ucas.ac.cn

dynamics, thereby mediating OC accumulation and stability in deep sediments, remain rarely investigated.

Hailed as the “Asian Water Tower”, the Qinghai-Xizang Plateau (QXP, also known as the Tibetan Plateau) encompasses over 100,000 km² of wetlands and serves as one of the largest carbon reservoirs in China¹⁹. Most studies regarding these critical alpine wetlands have prioritized the surface soil carbon pool. Limited studies on deep sediment OC have primarily focused on carbon accumulation rates and timelines, suggesting that sediment OC formation in most wetlands dates back to the early Holocene^{20–22}. However, the rapidly rising temperatures^{23,24}, intensifying climatic extremes²⁵, and earthquake-induced fractures²⁶ have significantly elevated the risk of decomposition and release of deep OC, which was previously buried in cold, anoxic environments and is generally considered highly recalcitrant. Such processes are likely to generate positive feedback on global warming and urgently require in-depth investigation.

To address these knowledge gaps, we performed 42 sediment cores (each ranging from 5.7 m to 23.5 m in depth) across seven typical wetlands in central and southern QXP to assess the vertical distribution of sediment OC content and the OC stocks in deep sediments (Fig. 1). Moreover, we selected the sediment core Naqu4 (NQ4) with the most continuous sedimentary sequence to investigate sediment OC stability and historical drivers by integrating Fourier-transform infrared spectroscopy (FTIR), X-ray fluorescence (XRF), and grain size analysis. Our findings uncover that deep sediments (over 1 m and above the first aquiclude; see Methods) store ~70% of the total OC in alpine wetlands, a substantial portion of which is labile. Both historical warming and an intercalated sedimentary structure, formed by silt and fine-grained clay, are essential drivers of these deep-buried labile OC pools.

Results and discussion

Sediment OC content and stocks

Across seven wetlands, OC content generally exhibited an overall increasing trend since the Holocene (Fig. 2). Surface sediments (< 1 m) contain the highest OC content, reaching up to 142.69 g kg⁻¹, which aligns with the conventional understanding that the uppermost layers serve as primary OC reservoirs due to continuous organic matter deposition and constraints on microbial decomposition^{2–4}. However, our results challenged the previous understanding that OC content declines monotonically with depth^{6,27}. In our study, many deep-sediment layers exhibited OC content comparable to or exceeding surface sediments. For instance, at depths of 3.2 m in NQ4 and 2.4 m in Dangqu (DQ), OC content reached 144.64 ± 5.04 g kg⁻¹, surpassing surface layer content of 133.65 ± 25.63 g kg⁻¹ (*p* = 0.04). Similar results were also observed at depths of 1.2 m, 2.6 m, and 4 m in Shenzha (SZ), as well as at ~15.5 m in ZB, where the average deep-sediment OC content accounts for 72.63% to 146.80% of those in the surface layer. These findings are consistent with observations by Chen et al.²⁸, who reported elevated OC concentrations in deep-sediment layers (2–5 m) of the Zoige peatland on the QXP. The long-term preservation of high OC content in deeper sediments likely results from substantial historical organic matter deposition, coupled with burial conditions that suppress decomposition. Low temperatures and oxygen levels create an environment that constrains microbial activity, thereby reducing OC turnover and promoting long-term carbon sequestration in wetland sediments^{28–30}.

Moreover, deep sediments stored a disproportionately large fraction of total OC stocks, contributing ~70% of the total active OC pool, extending from the surface to the lower boundary of unconfined aquifers (Table 1). Within this depth range, deep-buried OC may be released into surrounding

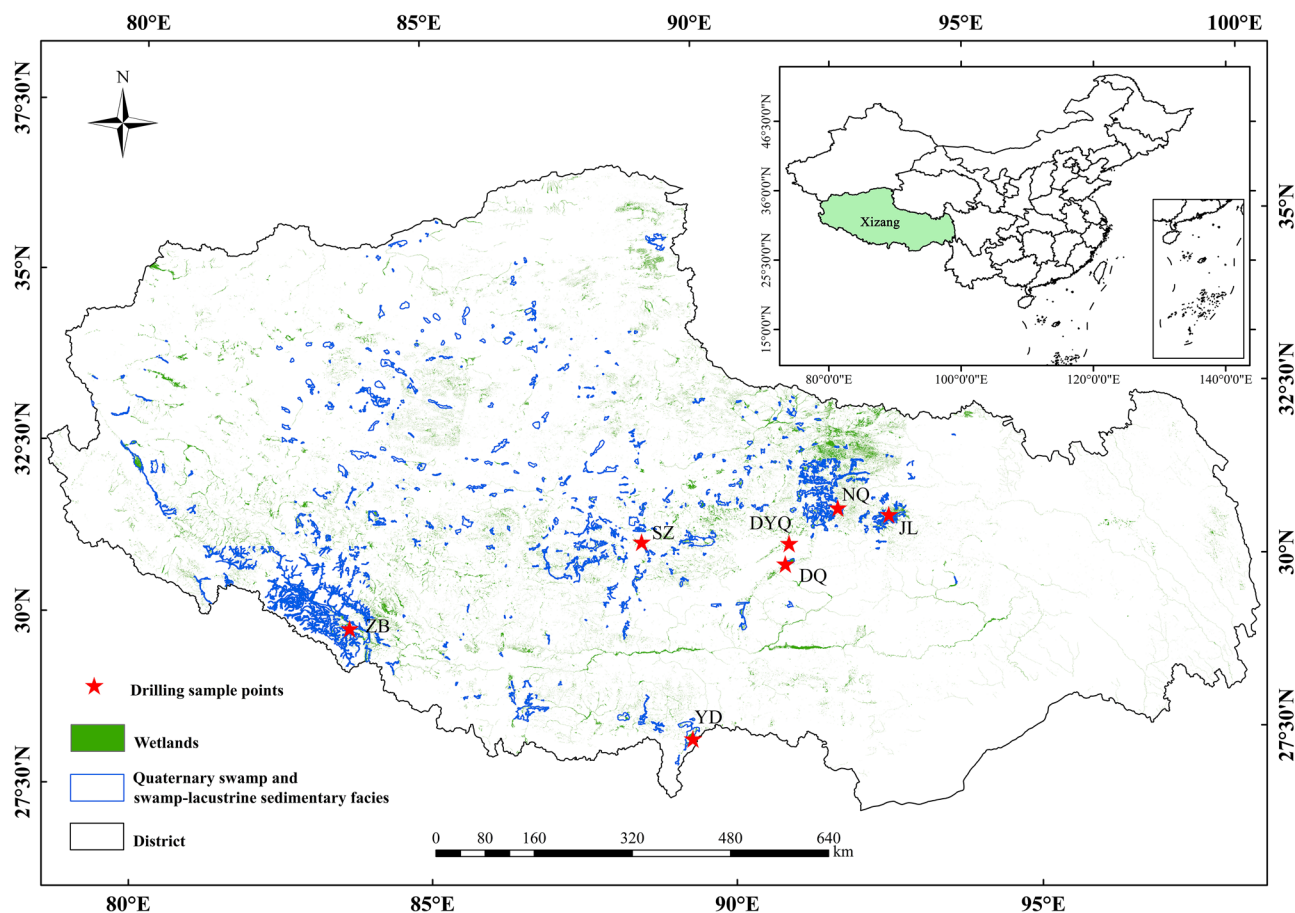


Fig. 1 | Drilling location map. The selected seven wetlands are marked by red stars. The distribution of alpine wetlands is highlighted in green⁶⁵, while Quaternary swamp and swamp-lacustrine sedimentary facies are represented in blue⁶⁶.

The wetlands include Naqu (NQ), Niyagu (NYQ), Shenzha (SZ), Dangqu (DQ), Yadong (YD), Jiali (JL), and Zhongba (ZB). The inset map on the upper right highlights the location of Xizang Autonomous Region within China (green shading).

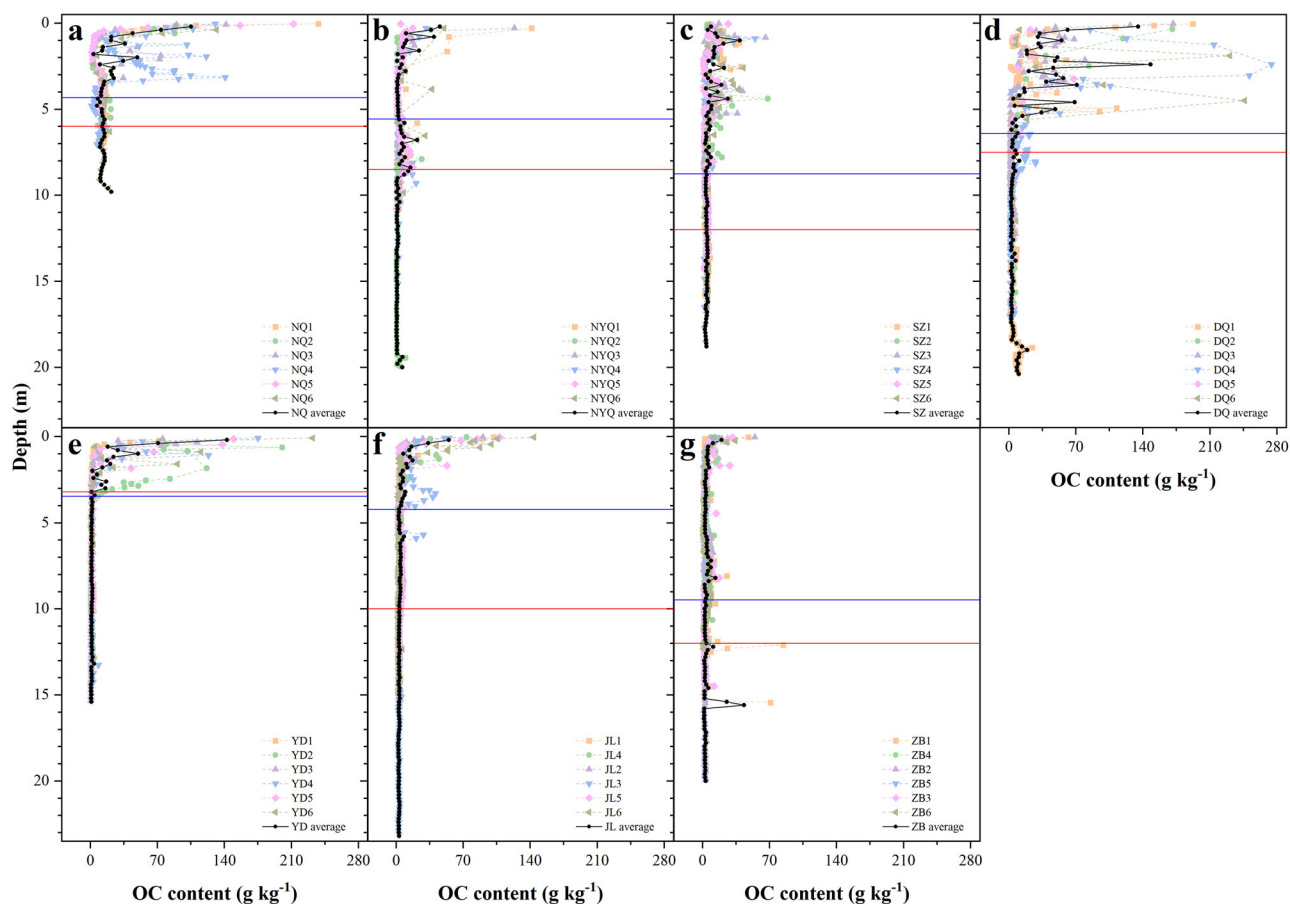


Fig. 2 | Vertical distribution of organic carbon (OC) content in the seven typical wetlands on the Qinghai-Xizang Plateau. Naqu (NQ) (a), Niyaqu (NYQ) (b), Shenzha (SZ) (c), Dangqu (DQ) (d), Yadong (YD) (e), Jiali (JL) (f), and Zhongba (ZB) (g). The solid blue line indicates the sediment depth corresponding to the onset of the Holocene. The solid red line indicates the sediment depth corresponding to the bottom boundary of the unconfined aquifer.

Table 1 | Organic carbon (OC) stocks and their relative proportions at different sediment depths (mean ± 95% CI) in typical wetlands

Site	Area (km ²)	Bottom boundary (m)	Holocene location (m)	OC stocks (Tg)				Relative proportion (%)		
				0–1 m	1 m - Holocene location	Holocene location - bottom	Total	0–1 m	1 m - Holocene location	Holocene location - bottom
NQ	0.52	6.0	4.33	0.03 ± 0	0.04 ± 0	0.02 ± 0	0.09 ± 0	33.19	47.39	19.42
NYQ	9.50	8.5	5.65	0.44 ± 0.02	0.70 ± 0.03	0.35 ± 0.01	1.49 ± 0.05	29.29	47.12	23.59
SZ	69.06	12	8.75	1.53 ± 0.03	6.77 ± 0.14	1.56 ± 0.02	9.86 ± 0.18	15.52	68.67	15.81
DQ	164.20	7.5	6.42	9.57 ± 0.75	47.93 ± 5.48	1.65 ± 0.03	59.16 ± 5.81	16.18	81.02	2.79
YD	340.21	3.2	3.44	22.32 ± 1.53	18.52 ± 1.44	-	41.27 ± 2.73	54.08	43.83	-
JL	843.42	10	4.22	30.55 ± 1.37	36.98 ± 0.84	34.98 ± 0.44	102.51 ± 2.35	29.8	36.07	34.12
ZB	995.61	12	9.47	16.04 ± 0.31	59.41 ± 0.81	13.69 ± 0.19	89.14 ± 1.28	17.99	66.65	15.36

CI confidence interval, NQ Naqu, NYQ Niyaqu, SZ Shenzha, DQ Dangqu, YD Yadong, JL Jiali, ZB Zhongba, respectively. The bottom boundary is defined as the burial depth of an impermeable or weakly permeable clay layer. In Yadong, since the bottom boundary lies above the Holocene depth, the proportion of deep-sediment OC stocks below 1 m was not included in the calculation.

surface water bodies and subsequently enter the atmosphere due to intense hydrological processes in the shallow aquifers of wetlands. These results align with many previous studies, which reported that deep sediment OC stocks could account for more than ~60% of the total OC storage, underscoring their substantial yet often overlooked role in carbon sequestration^{27,31}. Such findings emphasize that deep sediments play a far more significant role in long-term carbon sequestration than previously recognized on the QXP. Current carbon stock assessments and carbon cycle models predominantly focus on surface sediments, potentially leading to an underestimation of wetland

carbon storage capacity^{3,5,6}. Given this gap, understanding the accumulation mechanisms and stability of deep-sediment OC is critical for assessing future climate change impacts. Hence, we analyzed these aspects using the most continuous sedimentary sequence (NQ4; see “Methods”).

The OC accumulation and its associations with historical climate changes

The NQ4 sediment core, located near the Naqu River, is characterized by extensive Quaternary swamp and swamp-lacustrine sedimentary facies

beneath the modern wetlands. Chronological analysis indicated a maximum age of 35.716 ± 1.04 cal ka BP (where 0 cal ka BP corresponds to AD 1950) (Table S2 and Figure S1a). The Holocene sediment accumulation rate (SAR) averaged approximately ~ 0.745 mm a^{-1} (Figure S1b).

The OCAR, derived from sediment OC content and age, fluctuated since the Holocene (Fig. 3a). This trend closely paralleled variations in Ca/Si and Mo inc/Al ratios ($r = 0.38$ and $p < 0.01$, $r = 0.41$ and $p < 0.05$, respectively; Figure S3). In contrast, OCAR exhibited an inverse relationship with Rb/Sr and Fe/Ca ratios ($r = -0.46$ and $p < 0.01$, $r = -0.39$ and $p < 0.05$, respectively; Fig. 2a and S3). During the early Holocene (8.2–11.7 cal ka BP), OCAR remained relatively low (~ 4.87 g $m^{-2} a^{-1}$), coinciding with reduced Ca/Si and Mo inc/Al values and elevated Rb/Sr and Fe/Ca ratios. These geochemical patterns suggest that arid conditions prevailed in Xizang,

leading to a slower sediment accumulation rate within oxidative depositional environments³². Consistent with paleoclimate records from other wetlands on the QXP during the same period, the mean annual temperature (MAT) at Ngamring Co³³ was 5.96 ± 0.76 °C lower than modern levels, and the $\delta^{18}O$ value at Selin Co³⁴ was positive (average of -3.41 ‰) (Fig. 4). This regional pattern confirms that the early Holocene was dominated by a cold and dry climate, which suppressed wetland productivity and organic carbon accumulation. In contrast, from the middle to late Holocene (after 8.2 cal ka BP), OCAR exhibited a multimodal trend, with pronounced peaks at ~ 5.2 cal ka BP (61.32 g $m^{-2} a^{-1}$), ~ 2.9 cal ka BP (66.37 g $m^{-2} a^{-1}$), ~ 1.9 cal ka BP (52.31 g $m^{-2} a^{-1}$), and ~ 1.1 cal ka BP (40.35 g $m^{-2} a^{-1}$). These peaks coincided with the highest Ca/Si and Mo inc/Al values and relatively low Rb/Sr and Fe/Ca ratios, indicating a climatic shift toward warmer and wetter

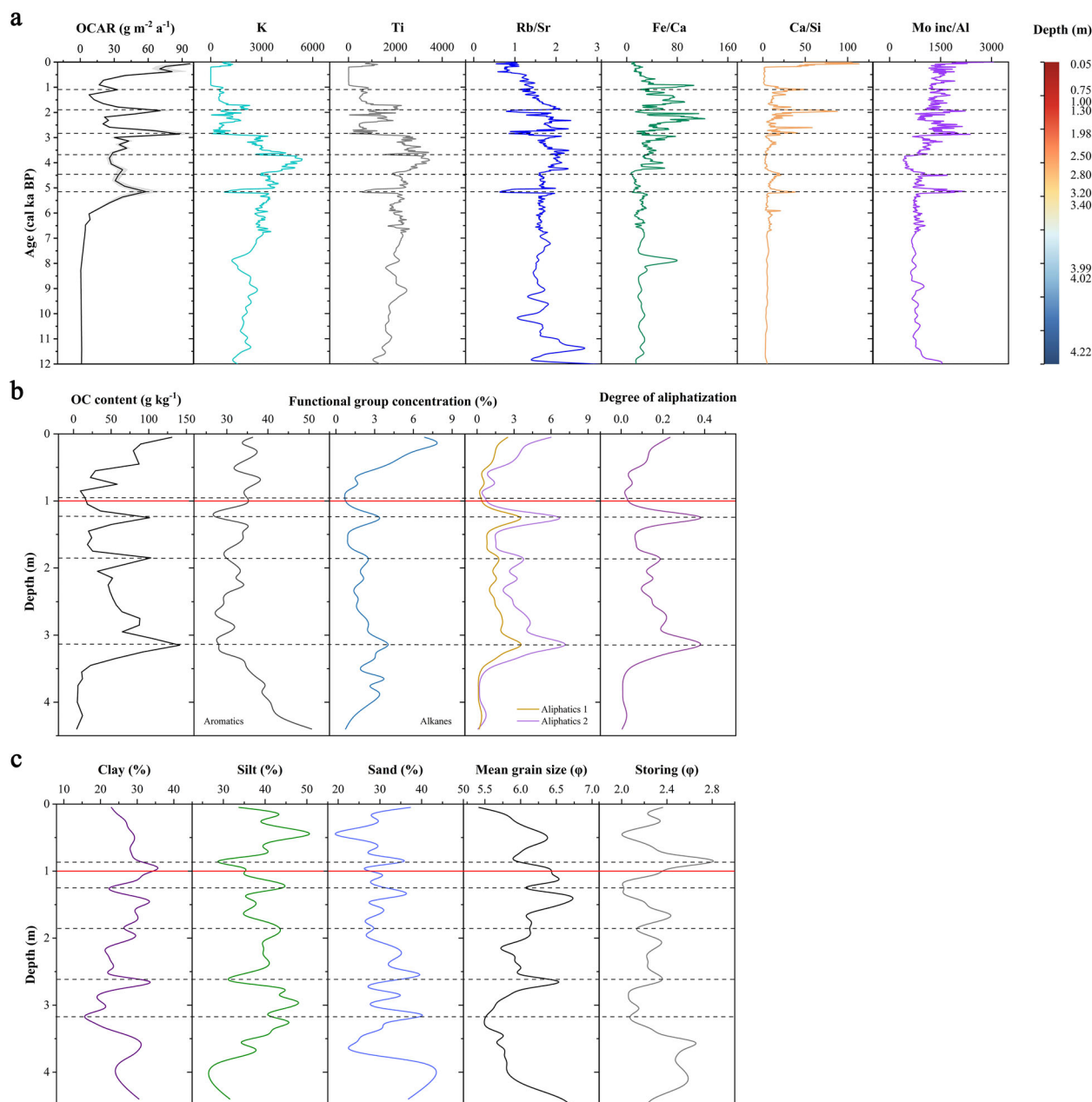
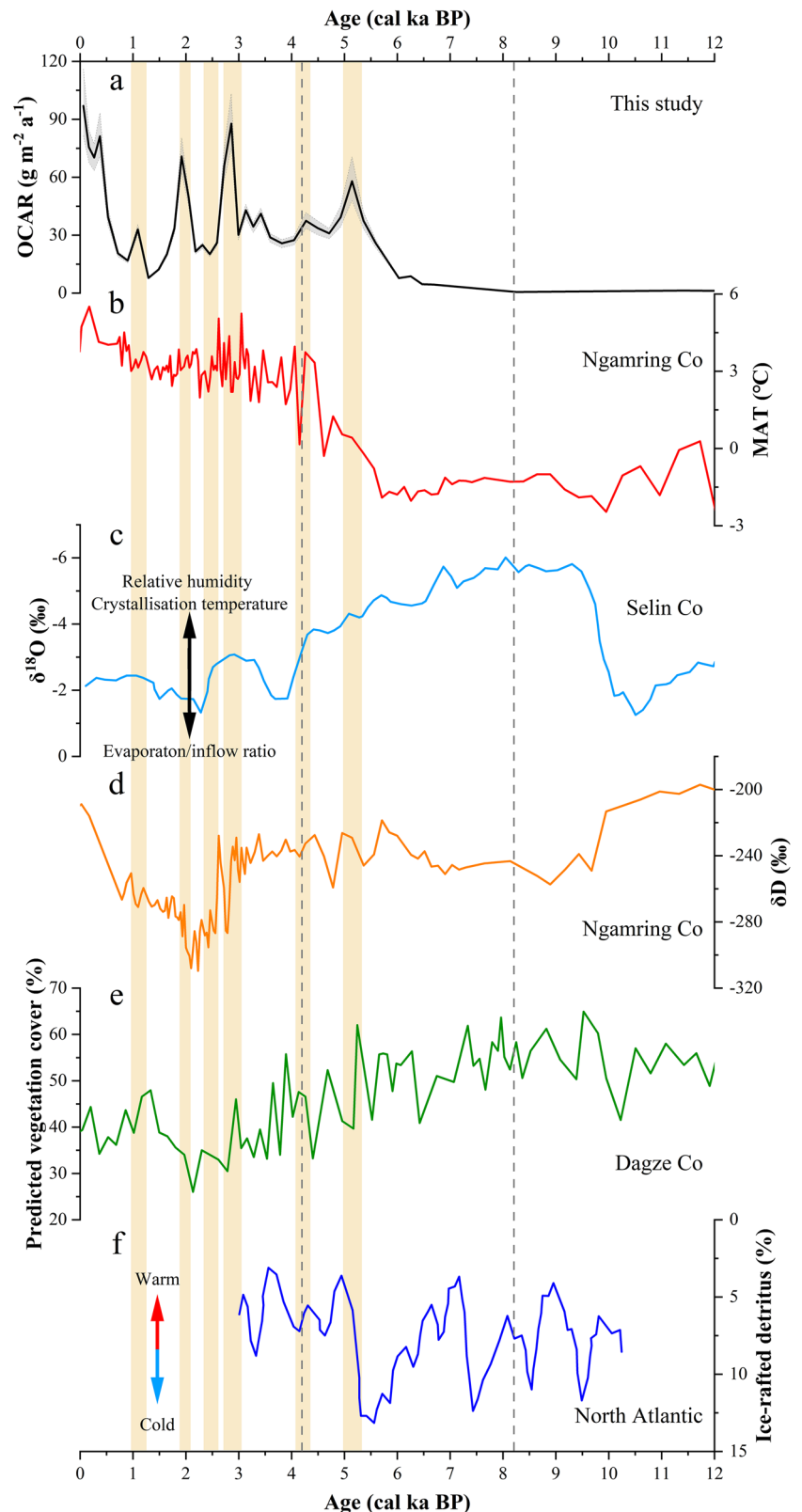


Fig. 3 | Vertical distribution of organic carbon accumulation and associated sedimentary properties in core Naqu4. Organic carbon accumulation rate (OCAR) and XRF-derived geochemical proxies (K, Ti, Rb/Sr, Fe/Ca, Ca/Si, Mo inc/Al) (a); FTIR-derived functional groups (aromatic, alkane, and aliphatic) and the degree of

aliphization (DA) in organic matter (b); and Sediment texture parameters, including clay, silt, and sand contents, mean grain size, and sorting (c). The red lines separate the surface (< 1 m) from deep sediments.

Fig. 4 | Climate records from the central Qinghai-Xizang Plateau and monsoon-dominated regions since the Holocene. The dataset includes the organic carbon accumulation rate (OCAR) from the NQ4 core (this study) (a), mean annual temperature (MAT) from Ngamring Co³³ (b), $\delta^{18}\text{O}$ from Selin Co³⁴ (c), and δD from Ngamring Co³³ (d). Reconstructed vegetation cover based on pollen data from Dagze Co³⁶ (e) and drift ice record from the North Atlantic³⁷ (f) are also shown.



conditions. These warm-wet phases enhanced wetland productivity, increasing the input of organic matter, while the generally cold conditions of the QXP further suppressed microbial decomposition, collectively fostering significant OC accumulation³⁵. This transition is further corroborated by lacustrine sedimentary records from Dagze Co³⁶ and Ngamring Co³³. For example, during the Holocene Thermal Maximum phase at ~5.2 cal ka BP,

the vegetation cover reconstructed from Dagze Co pollen data reached a peak of 62.03%³⁶, while the δD record from Ngamring Co sediments showed a relative enrichment value of -220‰ ³³. Additionally, the OCAR peak during this period was temporally coupled with the drift ice record from the North Atlantic (a low value of 3.62%, phase difference $< \pm 0.1$ ka)³⁷, further suggesting a possible remote correlation between high-latitude climate

forcing and carbon dynamics on the QXP. These findings underscore the essential role of historical climate in forming wetland carbon pools. Accordingly, our analyses further investigated its influences on carbon stability.

The OC stability in deep sediments

The aliphatic content and its ratio to aromatic content are widely recognized indicators for characterizing OC stability^{9,38}. Our results indicated that the relative content of aliphatic functional groups (1420/1040) and the degree of aliphaticization [(2850 + 2919)/790] closely tracked variations in deep-sediment OC content since the Holocene (Fig. 3b). Both parameters exhibited a significant positive correlation with OC content, with correlation coefficients of 0.94 and 0.93 ($p < 0.001$ and $p < 0.001$, respectively; Figure S3). These findings suggest that OC-rich layers, particularly in deep sediments, contain higher levels of labile OC. However, in contrast to the observations of Routh et al.⁹ and Kalisz et al.^{10,11}, our results did not show a continuous increase in labile OC with depth. Instead, labile OC fluctuated, with markedly higher degrees of aliphaticization observed at specific depths, particularly at ~1.3 m and ~3.2 m. The degrees of aliphaticization at these depths reached 0.49 and 0.43, respectively, substantially exceeding the peak value of 0.23 observed in surface sediments. These results highlight a more complex relationship between deep-sediment OC stability and depth, suggesting the existence of other drivers, such as historical climate.

Furthermore, we identified sedimentary structure as a crucial driver of OC stability in deep sediments. Variations in sediment density (BD), validated using X-ray tomography (XRT) intensity as an independent physical proxy (linear negative correlation; $R^2 = 0.29$, $p < 0.001$), reflect temporal shifts in sediment composition and packing (Figures S6, S7). Generally, clay content increased with depth within the 0–1 m range and below 3 m, while fluctuating between 1–3 m. In contrast, silt and sand fractions peaked at depths of ~1.3 m (~1.9 cal ka BP) and ~3.2 m (~5.2 cal ka BP), and exhibited a clear trend toward finer grain sizes (average grain size increasing from ~5.5 ϕ to ~6.7 ϕ) above these depths, accompanied by moderate sorting (1.9–2.4 ϕ), with both depths covered by high-clay layers (Fig. 3c). This distinct stratigraphic pattern suggests alternating depositional regimes linked to climatic variability^{10,28}. During warm-wet periods (e.g., ~5.2 and ~2.9 cal ka BP), enhanced runoff led to coarser silt deposition with higher OC input, forming low-density layers (BD < 0.9 g cm⁻³). During dry-cold phases (e.g., ~4.2 and ~1.3 cal ka BP), fine-grained clay deposition dominated, increasing BD and limiting oxygen diffusion. The overlying clay layers formed a protective intercalated structure that limited oxygen exposure and physical disturbance, thereby enhancing OC preservation. Moreover, a strong correlation was observed between the degree of aliphaticization and clay or silt content ($r = -0.59$ and $p < 0.01$, $r = 0.54$ and $p < 0.01$, respectively; Figure S3), suggesting that the intercalation of clay and silt layers played a critical role in facilitating the accumulation and preservation of labile OC in deep sediments.

Drivers of the OC stability in deep sediments

To integrate the abovementioned findings, the degree of aliphaticization showed significant correlations with OCAR ($R^2 = 0.56$, $p < 0.001$), clay ($R^2 = 0.33$, $p < 0.001$), and silt ($R^2 = 0.21$, $p = 0.002$) (Fig. 5a). The OCAR was positively correlated with MAT ($R^2 = 0.26$, $p < 0.001$) and silt ($R^2 = 0.29$, $p < 0.001$), and negatively correlated with sediment age ($R^2 = 0.33$, $p < 0.001$), depth ($R^2 = 0.21$, $p = 0.002$), and clay ($R^2 = 0.22$, $p = 0.002$) (Fig. 5b). A partial least squares path modeling (PLS-PM) was performed to identify the key drivers of OC stability in deep sediments. The analysis revealed OCAR, MAT, and silt content as key factors influencing sediment OC stability (Fig. 6).

The high path coefficient from OCAR to sediment OC stability (0.99, $p < 0.001$) suggests that variations in carbon input predominantly control the preservation of labile OC pools. The MAT indirectly enhanced sediment OC stability by increasing OCAR, with a statistically significant path coefficient of 0.99 ($p < 0.001$). This result is consistent with previous studies, which reported that elevated OCAR in northern peatlands was closely

linked to the warm Holocene climate^{13,20,21}. During that period, rapid OC accumulation occurred alongside suppressed decomposition under anaerobic conditions (often indicated by high Mo inc/Al ratios; Fig. 3a), facilitating the burial of a substantial proportion of labile carbon in these sediment layers^{39,40}.

Sediment structure exerts a key physical control over the long-term stability of buried OC. Silt content enhances stability primarily by increasing OCAR (path coefficient = 0.51, $p < 0.001$), likely due to its association with high sedimentation rates and rapid burial that limit oxygen exposure. In contrast, although negatively correlated with OCAR (Fig. 5b), clay content supports OC stability by forming compact, low-porosity layers that reduce oxygen diffusion and protect the underlying higher proportion of labile OC. Additionally, these clay layers may promote the development of stable clay-humus complexes through interactions with organic matter^{41,42}. Over time, ongoing deposition, burial, and compaction create increasingly oxygen-limited conditions above the rapidly accumulated silt layers, thereby suppressing decomposition and enhancing labile OC preservation. Such an intercalated sedimentary structure is particularly pronounced in wetlands and coastal tidal flats with high sedimentation rates^{43,44}, representing an overlooked geological mechanism mediating wetland carbon stability.

Unlike many existing studies^{35,45}, we found that mean annual precipitation (MAP) negatively affected sediment OC stability by influencing OCAR, with a path coefficient of -0.46 ($p < 0.05$). This unusual finding is likely because the study site is a riverine wetland. High precipitation may induce strong hydrological disturbances (e.g., floods), undermining vegetation growth and reducing litter input²⁵. Besides, coarsening and poor sorting of sediment grains may promote oxygen and pore water exchange, leading to increased microbial aerobic respiration and lateral output of dissolved OC via surface runoff, consequently exacerbating OC losses and constraining sediment OC retention^{46,47}.

Among the factors examined, variables such as sediment age-depth and vegetation exhibited relatively minor effects ($p > 0.05$). Overall, sediment OC stability was primarily governed by sediment grain characteristics, mineral interactions, and the accessibility of OC to microbial degradation rather than by burial age or depth. Under the anoxic conditions prevalent in wetlands, the influence of age and depth on sediment OC oxidation was significantly attenuated^{10,11,48}. Notably, our study did not reveal a strong vegetation effect on OC stability, which contrasts with findings from many ecological studies^{49,50}. This is probably because the long-term cumulative effects of historical vegetation dynamics may have been weakened by surface sediment disturbances driven by climate variability or shifts in burial conditions. As a result, OC stability in deep sediments was more strongly dictated by mineral-associated protection mechanisms rather than by the residual influence of past vegetation^{51,52}. Additionally, the vegetation data used in this study were palynologically reconstructed, a method limited by low species resolution and potential biases from windborne pollen and spores. Future studies could involve sedimentary ancient DNA (sedaDNA) analysis to obtain a more accurate assessment of historical vegetation effects on OC accumulation^{53,54}.

Taken together, our findings highlight the complex interplay between the warm climate and sedimentation processes in shaping the long-term stability of sediment carbon pools in alpine wetlands.

Conclusions

This study on the Qinghai-Xizang Plateau reveals that, unlike well-studied alpine grasslands, OC in wetlands does not decline linearly with depth. Deep sediments in the unconfined shallow aquifer store ~70% of the total OC, much of which is labile, challenging the prevailing assumption that OC in deep soils is both scarce and highly recalcitrant. While temperature remains a crucial driver of deep-sediment OC accumulation and chemical stability, our work introduces an overlooked geological mechanism in which the “clay-silt-clay” sedimentary structure mediates OC stability. These findings underscore the need to include these long-neglected labile carbon pools in climate change research and assessments, particularly as rising temperatures²⁴, intensifying extreme precipitation events⁵⁵, and earthquake-

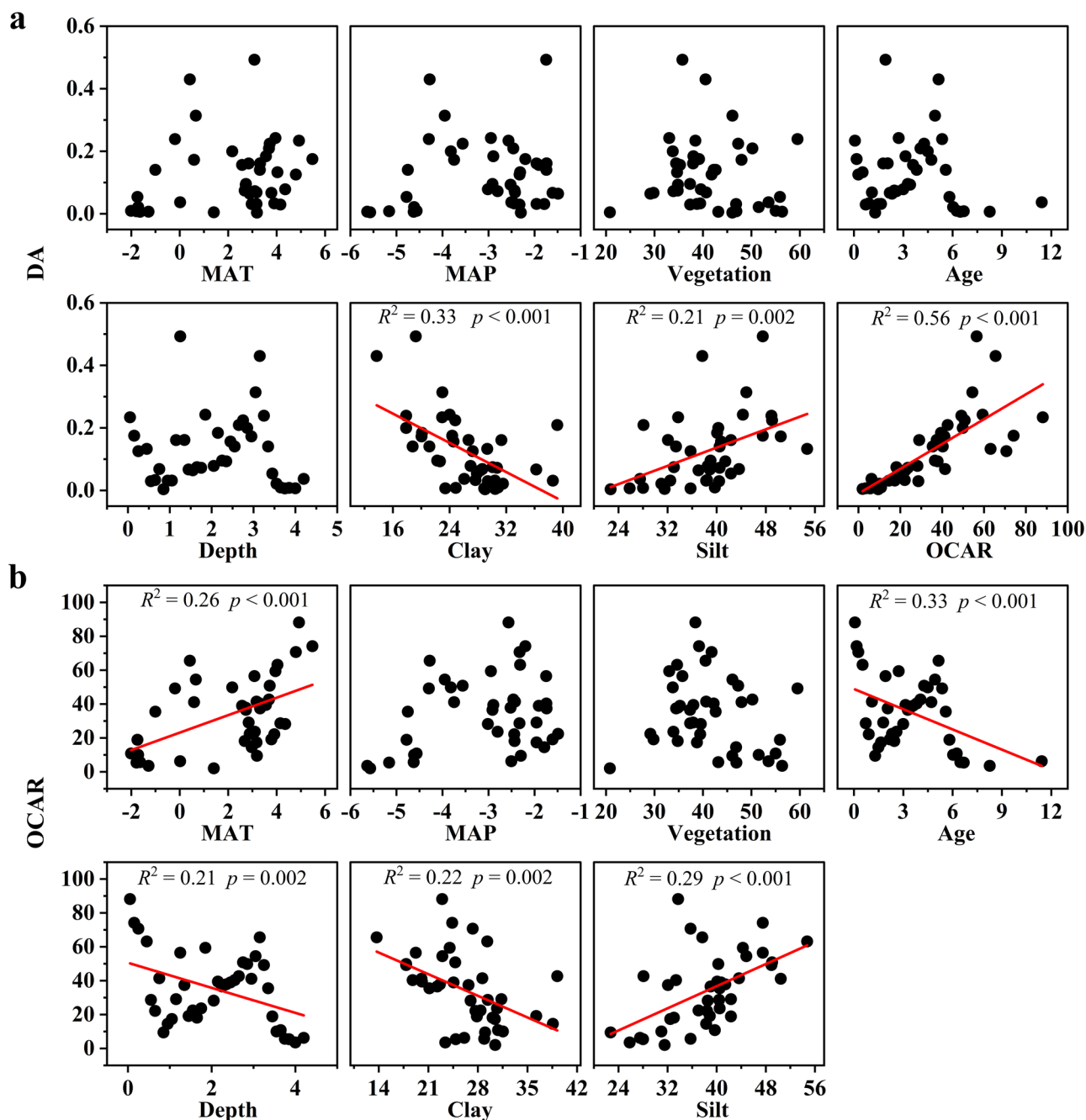


Fig. 5 | Relationships of organic carbon properties with environmental and sedimentary variables. Relationships between the degree of aliphaticization (DA) and its potential influencing variables (a); and Relationships between organic

carbon accumulation rate (OCAR) and its potential influencing variables (b). MAT: mean annual temperature; MAP: mean annual precipitation; Vegetation: vegetation cover.

induced fractures²⁶ on the QXP may trigger deep OC decomposition, thereby exacerbating global warming. Recognizing the susceptibility of these deep-sediment OC pools to environmental perturbations is crucial for refining predictions of carbon cycling and their potential influence on future climate trajectories. This requires interdisciplinary research across ecology, hydrology, geochemistry, and paleoclimatology, as well as new methods such as sedimentary ancient DNA analysis.

Methods

Study area and sampling methods

The study was conducted in the Xizang Autonomous Region of China, located between 78°25'–99°06'E and 26°50'–36°53'N, with an average altitude of ~4500 m. The region experiences a highly variable climate,

characterized by cold and dry conditions in the northwest, and warmer and more humid conditions in the southeast. The annual temperature ranges from –2.8 to 11.9 °C, while precipitation varies from 74.8 mm to 901.5 mm. Dominant vegetation species in the region include *Kobresiatibetensis*, *Carex parvula* O. Yano, and *Bistorta vivipara* (L.) Gray.

Fieldwork was conducted across seven typical alpine wetlands located in Naqu (NQ), Niyaqu (NYQ), Shenzha (SZ), Dangqu (DQ), Yadong (YD), Jiali (JL), and Zhongba (ZB) (Fig. 1, Table S1), most of which were situated within national parks or nature reserves. No signs of land cultivation, drainage, or other disturbances were observed in the wetland areas of the drilling sites. The drilling depths ranged from 5.7 m to 23.5 m, penetrating the unconfined groundwater layer and exposing one or more confined groundwater layers. At each site, a total of six duplicate cores (90 mm in

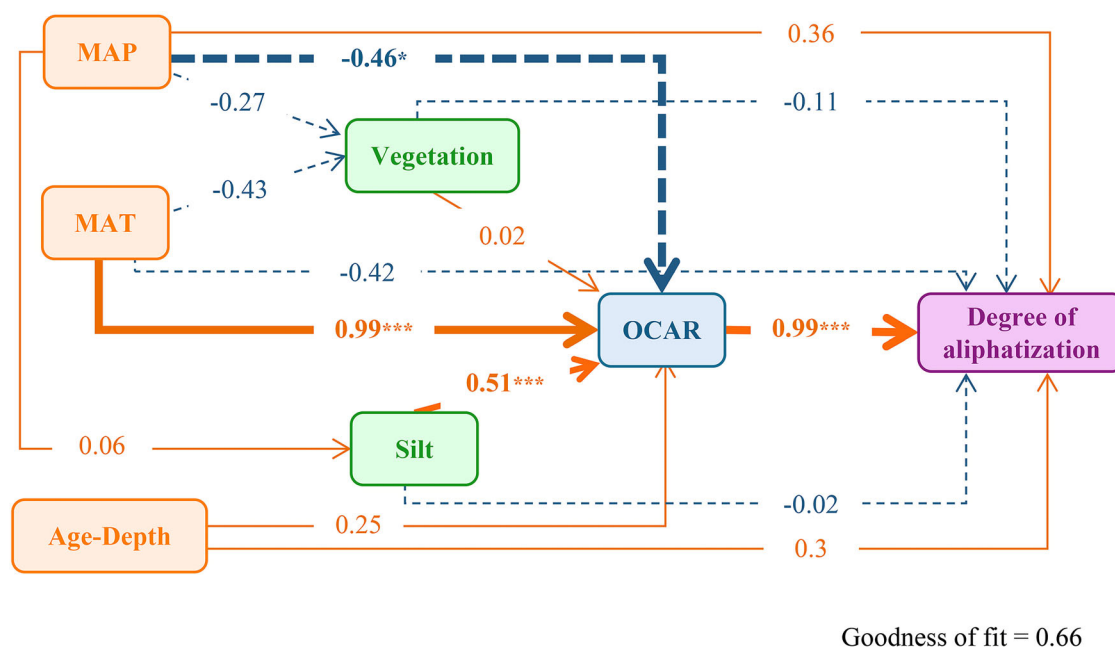


Fig. 6 | Partial least squares path modeling (PLS-PM) illustrates the effects of climatic variables and burial conditions on organic carbon stability since the Holocene. MAP mean annual precipitation, MAT mean annual temperature, OCAR organic carbon accumulation rate. Significance levels are marked as follows:

* $p < 0.05$, ** $p < 0.01$, and *** $p < 0.001$. Orange solid lines represent positive effects, while blue dashed lines indicate negative effects. Line thickness reflects the interaction strength between variables.

diameter) were collected at ~100 m intervals. The collected cores were cryosealed for transport to the laboratory, where they were longitudinally split and photographed. Subsamples were then dried, weighed, ground, and sieved through a 2 mm sieve to remove visible stones, while retaining plant debris. The physicochemical properties of the samples, including organic carbon (OC) content and grain size, were analyzed. The OC content was determined using the dichromate oxidation-colorimetric method⁵⁶. To minimize potential interference from Fe and Ca during OC determination by dichromate oxidation, phosphoric and sulfuric acids were added to chelate Fe^{3+} and prevent CaSO_4 precipitation, while blank corrections were applied to account for residual inorganic reducing agents. The grain size distribution was analyzed using a laser grain size analyzer (Microtrac S3500, USA), which provided data on the content of clay, silt, and sand. The mean grain size and sorting were calculated according to the method of Folk and Ward (1957)⁵⁷. To determine bulk density, 157 undisturbed sediment samples were collected from the vertical profiles of 21 sediment cores using a standard 100 cm³ container, accounting for over 10% of all core samples ($n = 1537$). Each sample was dried at 105 °C to a constant weight. Bulk density (BD) was then calculated as the ratio of dry mass to the volume of the container. Following previous research dealing with a large amount of drilling samples^{6,58}, an empirical model between bulk density and sediment OC content was established using these 157 samples ($R^2 = 0.54$; Figure S2). To assess model robustness, we recalibrated the BD-OC regression using 10-fold cross-validation ($R^2 = 0.54$; RMSE = 0.24 g cm⁻³) and performed residual diagnostics, which showed no systematic bias (Durbin-Watson test, $p = 0.36$). Notably, although cross-validation and Monte Carlo propagation confirmed its robustness, high- and low-OC extremes may still be underestimated. The model was then used to assess the BD of other sediment samples collected from the wetland cores.

Sediment dating

A total of 33 bulk sediment samples were selected from the seven wetlands for radiocarbon dating, with 3–10 samples per site according to the sediment depth and number of layers (Table S2). The samples were freeze-dried, sealed, and subsequently analyzed for radiocarbon content using accelerator mass spectrometry (AMS, USA) at the Miami Beta Analysis Company. The

obtained radiocarbon dates were calibrated using the IntCal20 calibration dataset⁵⁹. To construct an age-depth model for the entire depositional sequence, the calibrated dates were interpolated through a Bayesian approach. The depth marking the start of the Holocene was identified through this interpolation method. All analyses were performed using the Bacon 2.2 package in R 3.1.0⁶⁰.

Fourier-transform infrared spectroscopy (FTIR) for OC stability

The FTIR spectroscopy was conducted using a Cary 660 FTIR spectrometer (Agilent, USA) to analyze the molecular composition of natural organic matter in sediment samples. For analysis, each sample was prepared by mixing 2 mg of powdered sediment with 200 mg of FTIR-grade KBr, which was then pressed into 13 mm pellets. Spectra were obtained by averaging 32 scans per sample, with baseline corrections applied after subtracting the KBr background⁶¹. To precisely determine the wavenumber positions of characteristic peaks, we employed the baseline correction method and R script developed by Hodgkins et al.⁶¹. Peak intensities were then converted into relative abundances (Figure S5).

Four functional groups—aromatic, carbohydrate, alkane, and aliphatic—were analyzed to quantify the chemical stability of OC in the sediment samples. The relative content of each functional group was determined using specific peak ratios: aromatic (790/1040), alkane (1420/1040), and aliphatic (2850/1040 and 2919/1040). Additionally, the degree of aliphaticity was defined as the ratio of aliphatic to aromatic content, calculated as (2850/790 + 2919/790).

X-ray fluorescence (XRF) scanning for palaeoenvironmental and palaeoclimatic analyses

The sealed, segmented core samples were transported under cold-chain conditions to the Tibetan Plateau Key Laboratory of Earth System and Environment at the Institute of Tibetan Plateau Research, Chinese Academy of Sciences (ITP-CAS). Elemental composition, optical images, and radiographic images were analyzed using an Itrax XRF core scanner (Cox Itrax, Sweden). XRF scanning was performed using a 3 kW molybdenum target tube, operated at 30 kV and 50 mA, with a 1 mm resolution and a 15-second exposure time. X-ray imaging was captured at 30 kV and 10 mA, also at

1 mm resolution, with a 100 ms exposure time. The raw XRF spectra were processed using Q-Spec software to derive elemental peak area counts and X-ray transmission (XRT) intensity.

To analyze palaeoenvironmental and palaeoclimatic conditions, specific elemental ratios were selected, namely, potassium (K), titanium (Ti), rubidium to strontium (Rb/Sr), iron to calcium (Fe/Ca), calcium to silicon (Ca/Si), and molybdenum to aluminium (Mo inc/Al). These ratios serve as proxies for various environmental and climatic conditions: K and Ti indicate dust input and debris transport during dry periods; Rb/Sr and Fe/Ca reflect the dominance of chemical weathering over physical weathering, while Ca/Si indicates more substantial physical weathering; Mo inc/Al serves as a proxy for paleo-redox conditions^{62,63}.

Statistical analyses

In order to quantify the distribution and proportion of OC stocks in the sediments of alpine wetlands at various depths, we selected six duplicate core samples from seven representative wetlands in Xizang. These samples were analyzed for OC content and dated to determine the onset of the Holocene. Additionally, to explore the mechanisms underlying the formation of deep sediment OC, we selected core #4 from Naqu, an area characterized by extensive swamp sedimentation, swamp-lacustrine sedimentation, and a widespread distribution of modern wetlands. We analyzed the grain size, FTIR spectra, and XRF scans to assess OC stability, while incorporating palaeoenvironmental and palaeoclimatic data via partial least squares path modeling (PLS-PM) to identify the primary drivers. To minimize random errors, grain size and FTIR data were smoothed using a 5-point moving average, and XRF scan data were smoothed using a 20-point moving average.

Additional palaeoenvironmental and palaeoclimatic data were collected from the vicinity of NQ4 to serve as a reference. These data were used to examine relationships between mean annual temperature (MAT), mean annual precipitation (MAP), vegetation cover, sediment age and depth, clay and silt content, organic carbon accumulation rate (OCAR), and the degree of aliphaticization. Prior to multivariate modeling, we first performed simple linear regression analyses to evaluate the individual effects of each predictor variable on OCAR and the degree of aliphaticization. These regressions provided a quantitative basis for identifying potential key drivers, and the results are presented in Fig. 5. To reduce dimensionality and avoid collinearity, age and depth were subsequently merged via principal component analysis (PCA), with PC1, explaining 97.6% of the variance. Variance inflation factor (VIF) values for all retained predictors were below five. Building on these preparatory steps, PLS-PM was employed to identify the pathways influencing sediment OC stability. This method is particularly useful for demonstrating cause-and-effect relationships between observed and latent variables⁶⁴. The MAT data were obtained from Sun et al.³³, while the MAP data were derived from the $\delta^{18}\text{O}$ results presented by Gu et al.³⁴. Both climate variables were aligned with sample ages based on the established chronology. Vegetation data for the region were sourced from the reconstructed vegetation cover by Liu et al.³⁶ to ensure both accuracy and geographic relevance. Other parameters, including sediment age and depth, clay and silt content, OCAR, and degree of aliphaticization, were obtained through measurements conducted in this study. This statistical model was constructed using the “innerplot” function in the “plsmp” package⁶⁴. All statistical analyses were conducted in R version 4.1.3.

Organic carbon density (OCD) and OC stock for a given wetland sediment depth were calculated using Eqs. (1) and (2), respectively:

$$OCD = \frac{\sum_{i=1}^n OC_i \times BD_i \times H_i}{\sum_{i=1}^n H_i} \quad (1)$$

$$OC \text{ stock} = \frac{A \times \sum_{i=1}^n OC_i \times BD_i \times H_i}{1000} \quad (2)$$

where OC_i , OCD , BD_i , and H_i represent the average organic carbon content (g kg^{-1}), organic carbon density (kg m^{-3}), bulk density (g cm^{-3}), and equal interval depths (cm) of six cores in per wetland, respectively. The OC stock

represents the wetland sediment organic carbon stock (T_g), while A represents the wetland area (km^2).

Sediment accumulation rate (SAR) and OCAR were calculated using Eqs. (3) and (4), respectively:

$$SAR = \frac{H_i \times 10}{T_i} \quad (3)$$

$$OCAR = \frac{H_i \times BD_i \times OC_i \times 1000}{T_i} \quad (4)$$

where SAR, OCAR, and T_i represent the sediment accumulation rate (mm a^{-1}), OCAR ($\text{g m}^{-2} \text{a}^{-1}$), and the age at equal interval depths H_i (cm), respectively (Figure S1).

To propagate the model uncertainty to OC stock and OCAR, we ran 10,000 Monte Carlo iterations. In each iteration, we randomly sampled BD from its 95 % prediction interval (conditional on OC content) and recalculated OC stock and OCAR. The 2.5% and 97.5% quantiles of the resulting BD, OC stock, and OCAR sets provided 95% confidence intervals (Table 1 and Figure S7), and the resulting 95% confidence intervals for OC stock estimates ($\pm 1.56\%$ to $\pm 4.87\%$) were considerably lower than the spatial variability observed across sites (coefficient of variation = 44.14%), suggesting that the model-induced uncertainty is substantially smaller than natural heterogeneity.

Reporting summary

Further information on research design is available in the Nature Portfolio Reporting Summary linked to this article.

Data availability

The data supporting the findings of this study were deposited on figshare (<https://doi.org/10.6084/m9.figshare.30655583>).

Code availability

The R packages utilized in this study are publicly available, and no custom code was used.

Received: 25 April 2025; Accepted: 1 December 2025;

Published online: 16 December 2025

References

- Whiting, G. J. & Chanton, J. P. Greenhouse carbon balance of wetlands: methane emission versus carbon sequestration. *Tellus Ser. B-Chem. Phys. Meteorol.* **53**, 521–528 (2001).
- Stewart, A. J. et al. Revealing the hidden carbon in forested wetland soils. *Nat. Commun.* **15**, 726 (2024).
- Jackson, R. B. et al. The ecology of soil carbon: pools, vulnerabilities, and biotic and abiotic controls. *Annu. Rev. Ecol. Evol. Syst.* **48**, 419–445 (2017).
- Li, Y. et al. Factors controlling peat soil thickness and carbon storage in temperate peatlands based on UAV high-resolution remote sensing. *Geoderma* **449**, 117009 (2024).
- Hinson, A. L. et al. The spatial distribution of soil organic carbon in tidal wetland soils of the continental United States. *Glob. Change Biol.* **23**, 5468–5480 (2017).
- Ding, J. Z. et al. The permafrost carbon inventory on the Tibetan Plateau: a new evaluation using deep sediment cores. *Glob. Change Biol.* **22**, 2688–2701 (2016).
- Post, W. M., Emanuel, W. R., Zinke, P. J. & Stangenberger, A. G. Soil carbon pools and world life zones. *Nature* **298**, 156–159 (1982).
- Gitay, H. et al. in *Contribution of Working Group II to the IPCC Third Assessment Report: Impacts, Adaptation and Vulnerability* (eds J. J. McCarthy et al.) 235–342 (Cambridge University Press, 2001).
- Vasilevich, R., Lodygin, E., Beznosikov, V. & Abakumov, E. Molecular composition of raw peat and humic substances from permafrost peat

- soils of European Northeast Russia as climate change markers. *Sci. Total Environ.* **615**, 1229–1238 (2018).
10. Routh, J. et al. Multi-proxy study of soil organic matter dynamics in permafrost peat deposits reveal vulnerability to climate change in the European Russian Arctic. *Chem. Geol.* **368**, 104–117 (2014).
 11. Kalisz, B., Urbanowicz, P., Smólczyński, S. & Orzechowski, M. Impact of siltation on the stability of organic matter in drained peatlands. *Ecol. Indic.* **130**, 108149 (2021).
 12. Negassa, W., Acksel, A., Eckhardt, K.-U., Regier, T. & Leinweber, P. Soil organic matter characteristics in drained and rewetted peatlands of northern Germany: Chemical and spectroscopic analyses. *Geoderma* **353**, 468–481 (2019).
 13. Davies, M. A., Blewett, J., Naafs, B. D. A. & Finkelstein, S. A. Ecohydrological controls on apparent rates of peat carbon accumulation in a boreal bog record from the Hudson Bay Lowlands, northern Ontario, Canada. *Quat. Res.* **104**, 14–27 (2021).
 14. Gao, C. et al. High intensity fire accelerates accumulation of a stable carbon pool in permafrost peatlands under climate warming. *Catena* **227**, 107108 (2023).
 15. Zhang, T. et al. Warming-driven erosion and sediment transport in cold regions. *Nat. Rev. Earth Environ.* **3**, 832–851 (2022).
 16. García Lino, M. C. et al. Carbon dynamics in high-Andean tropical cushion peatlands: A review of geographic patterns and potential drivers. *Ecol. Monogr.* **94**, e1614 (2024).
 17. Heger, A., Becker, J. N., Vásconez, L. K. & Eschenbach, A. Drivers for soil organic carbon stabilization in Elbe River floodplains. *J. Plant Nutr. Soil Sci.* **187**, 346–355 (2024).
 18. Deiss, L. et al. Soil carbon fractions from an alluvial soil texture gradient in North Carolina. *Soil Sci. Soc. Am. J.* **81**, 1096–1106 (2017).
 19. Chen, H. et al. Carbon and nitrogen cycling on the Qinghai–Tibetan Plateau. *Nat. Rev. Earth Environ.* **3**, 701–716 (2022).
 20. Jones, M. C. & Yu, Z. Rapid deglacial and early Holocene expansion of peatlands in Alaska. *Proc. Natl. Acad. Sci. USA* **107**, 7347–7352 (2010).
 21. Loisel, J. et al. Insights and issues with estimating northern peatland carbon stocks and fluxes since the Last Glacial Maximum. *Earth-Sci. Rev.* **165**, 59–80 (2017).
 22. Juselius-Rajamäki, T., Vaeliranta, M. & Korhola, A. The ongoing lateral expansion of peatlands in Finland. *Glob. Change Biol.* **29**, 7173–7191 (2023).
 23. Gao, J., Yao, T. D., Masson-Delmotte, V., Steen-Larsen, H. C. & Wang, W. C. Collapsing glaciers threaten Asia's water supplies. *Nature* **565**, 19–21 (2019).
 24. Yao, T. et al. The imbalance of the Asian water tower. *Nat. Rev. Earth Environ.* **3**, 618–632 (2022).
 25. Feldman, A. F. et al. Plant responses to changing rainfall frequency and intensity. *Nat. Rev. Earth Environ.* **5**, 276–294 (2024).
 26. Shi, P. J. et al. Earthquakes have accelerated the carbon dioxide emission rate of soils on the Qinghai–Tibet Plateau. *Glob. Change Biol.* **31**, 10 (2025).
 27. Jobbágy, E. G. & Jackson, R. B. The vertical distribution of soil organic carbon and its relation to climate and vegetation. *Ecol. Appl.* **10**, 423–436 (2000).
 28. Chen, H. et al. The carbon stock of alpine peatlands on the Qinghai–Tibetan Plateau during the Holocene and their future fate. *Quat. Sci. Rev.* **95**, 151–158 (2014).
 29. Krauss, K. W. et al. The role of the upper Tidal Estuary in Wetland blue carbon storage and flux. *Glob. Biogeochem. Cycles* **32**, 817–839 (2018).
 30. Wang, Q. F. et al. The vertical distribution of soil organic carbon and nitrogen in a permafrost-affected wetland on the Qinghai–Tibet Plateau: implications for Holocene development and environmental change. *Permafrost. Periglac. Process* **33**, 286–297 (2022).
 31. Batjes, N. H. Total carbon and nitrogen in the soils of the world. *Eur. J. Soil Sci.* **65**, 10–21 (2014).
 32. Şenkul, Ç., Gürboğa, Ş., Doğan, M. & Doğan, T. High-resolution geochemical (μ XRF) and palynological analyses for climatic and environmental changes in lake sediments from Sultansazlığı Marsh (Central Anatolia) during the last 14.5 kyr. *Quat. Int.* **613**, 24–38 (2022).
 33. Sun, Z. et al. Changes in atmospheric circulation and glacier melting since the last deglaciation revealed by a lacustrine δ D record at Ngamring Co, the upper-middle Yarlung Tsangpo watershed. *Paleogeogr. Paleoclimatol. Paleoecol.* **598**, 11 (2022).
 34. Gu, Z., Liu, J., Yuan, B. & Liu, D. Monsoon variations of the Qinghai–Xizang Plateau during the last 12,000 years — geochemical evidence from the sediments in the Siling lake. *Chin. Sci. Bull.* **38**, 577–581 (1993).
 35. Wang, Y., Xia, A. & Xue, K. Cold and humid climates enrich soil carbon stock in the Third Pole grasslands. *Innovation* **5**, 100545 (2024).
 36. Liu, L. N. et al. Spatial and temporal variations of vegetation cover on the central and eastern Tibetan Plateau since the Last Glacial Period. *Glob. Planet. Change* **240**, 14 (2024).
 37. Bond, G. et al. Persistent solar influence on North Atlantic climate during the Holocene. *Science* **294**, 2130–2136 (2001).
 38. Peltre, C., Bruun, S., Du, C. W., Thomsen, I. K. & Jensen, L. S. Assessing soil constituents and labile soil organic carbon by mid-infrared photoacoustic spectroscopy. *Soil Biol. Biochem.* **77**, 41–50 (2014).
 39. Harris, L. I. et al. Permafrost thaw causes large carbon loss in boreal peatlands while changes to peat quality are limited. *Glob. Change Biol.* **29**, 5720–5735 (2023).
 40. Martínez Cortizas, A. et al. 9000 years of changes in peat organic matter composition in Store Mosse (Sweden) traced using FTIR-ATR. *Boreas* **50**, 1161–1178 (2021).
 41. Oades, J. M. The retention of organic-matter in soils. *Biogeochemistry* **5**, 35–70 (1988).
 42. Jacobs, P. M. & Mason, J. A. Impact of Holocene dust aggradation on A horizon characteristics and carbon storage in loess-derived Mollisols of the Great Plains, USA. *Geoderma* **125**, 95–106 (2005).
 43. Yamamoto, K. et al. Tropical peat debris storage in the tidal flat in northern part of the Bengkalis island, Indonesia. *MATEC Web Conf.* **276**, 06002 (2019).
 44. Yang, S. et al. Burial of organic carbon in Holocene sediments of the Zhujiang (Pearl River) and Changjiang (Yangtze River) estuaries. *Mar. Chem.* **123**, 1–10 (2011).
 45. Zhou, G. Y. et al. Climate and litter C/N ratio constrain soil organic carbon accumulation. *Natl. Sci. Rev.* **6**, 746–757 (2019).
 46. Li, Q.-W. et al. Precipitation patterns impact soil aggregates and organic carbon of an alpine wetland on the Qinghai–Tibetan Plateau. *Catena* **244**, 108249 (2024).
 47. Zhang, Y., Huang, X., Zhang, Z., Blewett, J. & Naafs, B. D. A. Spatiotemporal dynamics of dissolved organic carbon in a subtropical wetland and their implications for methane emissions. *Geoderma* **419**, 115876 (2022).
 48. Zhao, W. et al. Combination of mineral protection and molecular characteristics rather than alone to govern soil organic carbon stability in Qinghai–Tibetan plateau wetlands. *J. Environ. Manag.* **344**, 118757 (2023).
 49. Ding, Y. et al. The contribution of wetland plant litter to soil carbon pool: Decomposition rates and priming effects. *Environ. Res.* **224**, 115575 (2023).
 50. Xu, H. W. et al. Variation in soil organic carbon stability and driving factors after vegetation restoration in different vegetation zones on the Loess Plateau, China. *Soil Tillage Res.* **204**, 12 (2020).
 51. Malmer, N. & Wallén, B. Input rates, decay losses and accumulation rates of carbon in bogs during the last millennium: internal processes and environmental changes. *Holocene* **14**, 111–117 (2004).
 52. Ofiti, N. O. E. et al. Climate warming and elevated CO₂ alter peatland soil carbon sources and stability. *Nat. Commun.* **14**, 7533 (2023).

53. Liu, S. et al. Sedimentary ancient DNA reveals a threat of warming-induced alpine habitat loss to Tibetan Plateau plant diversity. *Nat. Commun.* **12**, 2995 (2021).
54. Zimmermann, H. H. et al. Sedimentary ancient DNA and pollen reveal the composition of plant organic matter in Late Quaternary permafrost sediments of the Buor Khaya Peninsula (north-eastern Siberia). *Biogeosciences* **14**, 575–596 (2017).
55. Fowler, H. J., Blenkinsop, S., Green, A. & Davies, P. A. Precipitation extremes in 2023. *Nat. Rev. Earth Environ.* **5**, 250–252 (2024).
56. Sims, J. R. & Haby, V. A. Simplified colorimetric determination of soil organic matter. *Soil Sci.* **112**, 137–141 (1971).
57. Folk, R. L. & Ward, W. C. Brazos River bar: a study in the significance of grain size parameters. *J. Sediment. Res.* **27**, 3–26 (1957).
58. Ezcurra, E. Precision and bias of carbon storage estimations in wetland and mangrove sediments. *Sci. Adv.* **10**, ead11079 (2024).
59. Reimer, P. J. et al. The IntCal20 Northern Hemisphere radiocarbon age calibration curve (0–55 cal kBP). *Radiocarbon* **62**, 725–757 (2020).
60. Blaauw, M. & Christen, J. A. Flexible paleoclimate age–depth models using an autoregressive gamma process. *Bayesian Anal.* **6**, 457–474 (2011).
61. Hodgkins, S. B. et al. Tropical peatland carbon storage linked to global latitudinal trends in peat recalcitrance. *Nat. Commun.* **9**, 3640 (2018).
62. Kylander, M. E., Ampel, L., Wohlfarth, B. & Veres, D. High-resolution X-ray fluorescence core scanning analysis of Les Echets (France) sedimentary sequence: new insights from chemical proxies. *J. Quat. Sci.* **26**, 109–117 (2011).
63. Glass, J. B. et al. Molybdenum geochemistry in a seasonally dysoxic Mo-limited lacustrine ecosystem. *Geochim. et. Cosmochim. Acta* **114**, 204–219 (2013).
64. Tenenhaus, M., Vinzi, V. E., Chatelin, Y.-M. & Lauro, C. PLS path modeling. *Comput. Stat. Data Anal.* **48**, 159–205 (2005).
65. Wu, B. Medium resolution land cover data of Qinghai-Tibet Plateau (1980–2020). National Tibetan Plateau Data Center. <https://doi.org/10.11888/Terre.tpd.c.300593> (2023).
66. China Geological Survey. Regional geological map of Xizang (1:250,000). National Geological Data Center. <https://www.ngac.cn/> (2005).

Acknowledgements

This work was supported by National Key Research and Development Program of China (Grant No. 2024YFF0808700), the National Natural Science Foundation of China (42407285), the Second Tibetan Plateau Scientific Expedition and Research Program (STEP) (Grant No. 2019QZKK0304), and the Key Science and Technology Program of Xizang (Grant No. XZ202101ZD0011G). We thank the Geothermal Geological Brigade (Tibet Bureau of Geology and Mineral Resources) for drilling and sampling, and Dr. Gao Shaopeng (Institute of Tibetan Plateau Research, CAS) for his supervision of the XRF scanning. No specific permissions were required for geological sampling. We sincerely thank the editor and the three anonymous reviewers for their constructive comments and insightful suggestions, which greatly improved the quality of this manuscript.

Author contributions

J.D. and Yanfen Wang conceived the study and designed the research protocol. Y.Y., Z.N., Y.Z., Z.W., L.M., Q.L., and Yu Wu carried out the field investigation and sample collection. Y.Y., X.W., Haijun Zhang, D.C., and C.G. performed data processing and statistical analyses. Y.Y. and X.W. drafted the initial manuscript. J.D., Hui Zhang, Y.H., H.N., K.X., and X.C. contributed to data interpretation and critically revised the manuscript. Yanfen Wang acquired funding for the project.

Competing interests

The authors declare no competing interests.

Additional information

Supplementary information The online version contains supplementary material available at <https://doi.org/10.1038/s43247-025-03081-8>.

Correspondence and requests for materials should be addressed to Jianqing Du or Xiaoyong Cui.

Peer review information *Communications Earth and Environment* thanks Alberto Araneda and the other, anonymous, reviewer(s) for their contribution to the peer review of this work. Primary Handling Editors: Somaparna Ghosh [A peer review file is available].

Reprints and permissions information is available at <http://www.nature.com/reprints>

Publisher's note Springer Nature remains neutral with regard to jurisdictional claims in published maps and institutional affiliations.

Open Access This article is licensed under a Creative Commons Attribution-NonCommercial-NoDerivatives 4.0 International License, which permits any non-commercial use, sharing, distribution and reproduction in any medium or format, as long as you give appropriate credit to the original author(s) and the source, provide a link to the Creative Commons licence, and indicate if you modified the licensed material. You do not have permission under this licence to share adapted material derived from this article or parts of it. The images or other third party material in this article are included in the article's Creative Commons licence, unless indicated otherwise in a credit line to the material. If material is not included in the article's Creative Commons licence and your intended use is not permitted by statutory regulation or exceeds the permitted use, you will need to obtain permission directly from the copyright holder. To view a copy of this licence, visit <http://creativecommons.org/licenses/by-nc-nd/4.0/>.

© The Author(s) 2025